# Crucial roles of eastward propagating environments in the summer MCS initiation over the U.S. Great Plains

Fengfei Song[1], Zhe Feng[1], L. Ruby Leung[1], Binod Pokharel[2], S.-Y. Simon Wang[2], Xingchao Chen[3], Koichi Sakaguchi[1], and Chichia Wang[2,4]

1. Atmospheric Sciences and Global Change Division, Pacific Northwest National Laboratory, Richland, Washington, USA

2. Department of Plants, Soils, and Climate / Utah Climate Center, Utah State University, Logan, Utah, USA

3. Department of Meteorology and Atmospheric Science, and Center for Advanced Data Assimilation and Predictability Techniques, The Pennsylvania State University, PA, USA

4. Central Weather Bureau, Taipei, Taiwan

Submitted to *Journal of Geophysical Research: Atmospheres*

**Corresponding author:**

Fengfei Song (Fengfei.Song@pnnl.gov)

**Key points:**

1. Summer MCSs in the U.S. Great Plains can initiate under unfavorable large-scale environments when favorable sub-synoptic forcing is present.

2. It propagates eastward for both large-scale and sub-synoptic environments, up to 25° west of and 36 hours prior to the MCS initiation.

3. About 30% of MPs from the Rocky Mountains are related to the initiation of intense MCSs under weak large-scale forcing.

## Abstract

This study aims at improving understanding of the environments supporting summer MCS initiation in the U.S. Great Plains. A self-organizing map analysis is conducted to identify four types of summer MCS initiation environments during 2004-2017: Type-1 and Type-2 feature favorable large-scale environments, Type-3 has favorable lower-level and surface conditions but unfavorable upper-level circulation, while Type-4 features the most unfavorable large-scale environments. Despite the unfavorable large-scale environment, convection-centered composites reveal the presence of favorable sub-synoptic scale environments for MCS initiation in Type-3 and Type-4. All four types of MCS initiation environments delineate a clear eastward propagating feature in many meteorological fields, such as potential vorticity, surface pressure and equivalent potential temperature, upstream up to 25° west of and ~36 hours before MCS initiation. While the propagating environments and local, non-propagating low-level moisture are important to MCS initiation at the foothill of the Rocky Mountains, MCS initiation in the Great Plains is supported by the coupled dynamical and moisture anomalies, both associated with eastward propagating waves. Hence, the MCSs initiated at the plains can produce more rainfall than those initiated at the foothill due to more abundant moisture supply. By tracking MCSs and mid-tropospheric perturbations (MPs), a unique type of sub-synoptic disturbances with Rocky Mountains origin, it is shown that ~30% of MPs is associated with MCS initiation, mostly in Type-4. Although MPs are related to a small fraction of MCS initiation, MCSs that are associated with MPs tend to produce more rainfall in a larger area with a stronger convective intensity.

## Plain Language Summary

During warm season (spring and summer), MCSs are often observed over the U. S. Great Plains and contribute considerably to the seasonal mean rainfall. However, compared to spring, the summertime MCS intiation is poorly understood, as large-scale environments are substantially weakened and the smaller-scale forcing is difficult to estimate based on the corase-resolution observations. Here, we use newly-developed MCS tracking dataset and newly-released ERA5 reanalysis dataset, both having high spatialtemporal resolutions to examine the summertime MCS initiation environments. We find that the eastward propagating environments at both large and smaller spatial scales, which can exist several days before the MCS initiation, play a crucial role in the MCS initiation. Both the propagating environments and local moisture are important for the MCS initiation at the foothill of Rocky Mountains, but at the central plains, the MCS initiation are associated with the propgating environments by coupling moisture and dynamical anomalies. Hence, the MCS rainfall is larger at the beginning several hours for those initiated at the plains compared to those initiated at the foothill due to more moisture supply. Finally, we quantify the contribution from one unique smaller-scale disturbances with Rocky Mountains origin to the summer MCS initiation.

## 1. Introduction

During the warm season (spring and summer), mesoscale convective systems (MCSs) are common features over the U.S. Great Plains (Houze, 2004, 2018; Schumacher & Rasmussen, 2020) and contribute substantially to the seasonal-mean and extreme rainfall (Feng et al., 2016, 2019; Fritsch et al., 1986; Nesbitt et al., 2006; Maddox et al., 1979; Schumacher & Johnson, 2005, 2006; Haberlie & Ashley, 2019). The role of synoptic environments in the warm-season MCS initiation has been extensively studied. Warm season MCSs are often initiated ahead of large-scale troughs at the upper troposphere with positive vorticity advection (e.g., Maddox, 1983; Anderson & Arritt 1998; Coniglio et al. 2004; Yang et al. 2017; Song et al., 2019) or beneath the upper-level ridge (e.g., Coniglio et al. 2004; Song et al. 2019), on the warm side of a synoptic front at the surface (e.g., Peters & Schumacher, 2014; Coniglio et al. 2010; Song et al. 2019), and/or at the exit region of the Great Plains low-level jet (GPLLJ) that converges moisture and destabilizes the atmosphere (e.g., Maddox, 1983; Anderson & Arritt 1998; Laing & Fritsch, 2000; Coniglio et al., 2010; Song et al. 2019).

However, compared to spring, synoptic forcing is considerably weaker so it plays a smaller role in summer MCS development (Song et al., 2019), which suggests a more important role of other forcings contributing to the development of summer MCSs. Our limited understanding of those forcings has implications, as summer MCSs are also more difficult to simulate and predict (Gao et al., 2017; Yang et al., 2017; Feng et al., 2018, 2021; Prein et al., 2020). Despite the weaker synoptic forcing, MCS intensity and precipitation amount can be stronger during summer than spring as noted by Feng et al. (2019), potentially posing larger threats of derechos, hails, tornadoes and flash flooding. Hence, there is an urgent need to improve our understanding on factors that contribute to the summertime MCS initiation.

Most previous studies did not distinguish the large-scale environments of MCSs between spring and summer over the Great Plains, but some studies noticed that summertime MCSs frequently occur under northwesterly flow associated with a high-pressure ridge to the west and a low-pressure trough to the east (e.g., Johns, 1982, 1984, 1993; Carbone et al., 2002; Wang et al., 2011a, b; Pokharel et al., 2019). Such large-scale environment is commonly thought to be unfavorable for MCS initiation due to the anticyclonic circulation aloft and the prevailing negative vorticity advection. Instead, sub-synoptic perturbations such as eastward-propagating waves (Li & Smith, 2010), residual short-wave troughs (Tuttle & Davis, 2013) and mid-tropospheric perturbations (MPs; Wang et al., 2011a, b; Pokharel et al., 2019), which appear to be embedded in the large-scale westerly or northwesterly flow, may support MCS initiation.

Using self-organizing map (SOM) analysis, Song et al. (2019) found a similar amount of summer MCS initiation in the U.S. Great Plains under either favorable or unfavorable large-scale environments. However, our current understanding on the role of sub-synoptic perturbations in the summertime MCS initiation is still limited, as it requires datasets with high spatiotemporal resolution. Using the North American Regional Reanalysis 32-km-resolution and 3-hourly data (NARR; Mesinger et al., 2006), Wang et al. (2011a, b) tracked MPs that originate from the Rocky Mountains and found that MPs exhibit a diurnal distribution with a primary peak at 12 UTC (early morning) and a secondary peak at 00 UTC (late afternoon). The early morning peak is linked to the lee side vorticity generation in the mid-troposphere, while the late afternoon peak is linked to a Charney-Stern type of instability in the mid-troposphere of the Rocky Mountains. As discussed by Wang et al. (2011a), the potential vorticity (PV) associated with the sub-synoptic scale perturbations are notably different from the PV generated by mature MCSs, which has an average wavelength around 400 km, much shorter than the sub-synoptic scale

perturbations with wavelength ranging from 700 to 1500 km. Wang et al. (2011a) also found that up to 60% of rainfall and storm reports over the northern plains in July and August could be associated with the presence of MPs. However, to what extent MPs are connected to organized storms like MCSs is not clear. Tuttle & Davis (2013) produced a 10-year (1998-2007) climatology of eastward traveling short waves with a wavelength of 1500 km using NARR and found that some of the short waves can be traced back to the Pacific Northwest as residual synoptic waves (Trier et al., 2006), which are different from the MPs that originate mainly from the Rocky Mountains. These studies suggested that short waves only play a secondary role in the diurnal cycle of precipitation over the Great Plains, as the latter is functional regardless of the presence of a short wave. Nonetheless, propagating short waves or other sub-synoptic perturbations connected to MCS initiation may provide a source of predictability for MCSs in the Great Plains. As MCSs contribute substantially to the diurnal cycle of precipitation, which represents a major challenge in climate modeling (e.g., Lin et al., 2017; Ma et al., 2018; Feng et al., 2021), it is important to quantify the relative contributions from different sources of sub-synoptic perturbations to summer MCS initiation for improving prediction and simulation of summertime MCSs in the U.S. Great Plains.

Taking advantage of high spatiotemporal MCS and MP tracking datasets and reanalysis products that have become available in recent years, this study aims at furthering our understanding of the large-scale vs. sub-synoptic scale environments supporting summer MCS initiation in the U.S. Great Plains. To examine the role of large-scale environment vs. sub-synoptic perturbations in MCS initiation, we use hourly MCS tracks (Feng 2019) and hourly/0.25° ERA5 reanalysis (Hersbach et al., 2020) to develop a 14-year (2004-2017) climatology of summertime MCS initiation environments and investigate their time evolution

before/after the MCS initiation. We also quantify the contribution of MPs to MCS initiation by analyzing hourly MP tracks in combination with hourly MCS tracks. The remainder of this paper is organized as follows: Section 2 introduces the MCS and MP tracking methods, the ERA5 reanalysis and our analysis methods. Section 3 discusses the main results, which include a comparison between large-scale composite and convection-centered composite, vertical structure of convection-centered environments, propagating features of convection-centered environments and the role of MPs in MCS initiation. Section 4 provides a summary and discussions.

## 2. Observational datasets and analysis methods

Here, we focus on June-July-August (JJA) of 2004-2017 for MCS and MP tracking and the use of the ERA5 reanalysis for the MCS environments.

### 2.1 MCS tracking

The MCS tracking dataset used here has hourly temporal resolution and 4 km spatial resolution (Feng 2019) based on MCS tracking using the FLEXible object TRacKeR (FLEXTRKR) algorithm (Feng et al., 2018) applied to three operational datasets: (1) a global merged geostationary satellite infrared brightness temperature ($T_b$) data produced by National Oceanic and Atmospheric Administration (NOAA) Climate Prediction Center (Janowiak et al., 2017); (2) a 3-dimensional mosaic National Weather Service Next-Generation Radar (NEXRAD) radar reflectivity data known as GridRad (Homeyer & Bowman 2017; Cooney et al., 2018); and 3) the Stage IV multi-sensor hourly precipitation dataset produced by the 12 River Forecast Centers in the continental United States (CONUS, Lin et al., 2011). The tracking algorithm first identifies large cold cloud systems with brightness temperature less than 241 K, then further identifies MCSs from these large cold cloud systems based on the radar reflectivity data and precipitation data. An MCS is defined as a cold cloud system greater than $6\times10^4$ km$^2$,

156 containing a precipitation feature with major axis length greater than 100 km, a convective
157 feature with radar reflectivity greater than 45 dBZ at all vertical levels, and precipitation feature
158 persisting for at least 6 h (Feng et al. 2019). Compared to other MCS tracking methods, which
159 use either cloud (e.g., Huang et al. 2018) or precipitation features (e.g., Stein et al. 2014) to
160 define MCSs, our method uses both the cloud and precipitation features to define MCSs, which
161 is more stringent and should be more accurate. Since the MCS tracking dataset uses satellite $T_b$,
162 MCS lifecycle includes initiation of isolated convection that eventually grow upscale into MCSs.
163 MCS initiation in this study refers to the first hour of convection detected ($T_b$ < 241 K) prior to
164 the formation of a mesoscale precipitation feature (> 100 km). See Feng et al. (2019) and Song et
165 al. (2019) for more details of the MCS tracking methods and MCS features.

166 **2.2 MP tracking**

167 MPs refer to the mid-tropospheric, sub-synoptic scale vortices that are embedded in the
168 northwesterly flow. They are generated over the Rocky Mountains and propagate across the
169 northern plains in the form of serial short-wave perturbations (Wang et al., 2011a, 2011b;
170 Pokharel et al., 2019). Using the hourly ERA5 reanalysis data, the criteria applied to track and
171 define MPs under the northwesterly background flows are modified from Pokharel et al. (2019)
172 that used 3-hourly NARR data. Three criteria are used to select MPs: first, cases with large-scale
173 upper-level troughs or low pressure are excluded; second, only cases with upper-level wind
174 speed greater than 15 m $s^{-1}$ are considered, as prevailing westerly wind plays an important role in
175 the propagation of MPs; third, only cases with high precipitable water (>24 mm) are considered,
176 as dry vortices (e.g., Davis et al., 2002) do not generate severe weather outbreaks (Wang et al.
177 2011a, 2011b). In addition to these three criteria, a given MP should last for at least 12

178 continuous hours. See Pokharel et al. (2019) for more details of the MP tracking methods and
179 MP features.

180 **2.3 ERA5 reanalysis datasets**

181 We also use the following hourly variables from ERA5 (Hersbach et al., 2020) with 0.25°
182 and hourly resolution to conduct SOM analysis and a composite analysis: vertical velocity,
183 geopotential height, temperature and specific humidity at all levesl; zonal and meridional wind at
184 200 hPa, 500 hPa and 925 hPa; potential vorticity (PV) at 200 hPa; surface pressure, surface air
185 temperature and dew-point temperature to calculate the surface equivalent potential temperature
186 ($\theta_e$).

187 **2.4 Self-organizing map (SOM) analysis and composite methods**

188 Similar to Song et al. (2019), SOM analysis is conducted to identify four types of large-
189 scale environments associated with summertime MCS initiation over the Great Plains. Here, we
190 select the zonal and meridional winds at three levels (925, 500 and 200 hPa) and the specific
191 humidity at two levels (925 and 500 hPa) over the domain (20°-55°N, 70°-110°W) at the time of
192 MCS initiation to conduct the SOM analysis. As we focus on the environments conducive to
193 MCS development, only the environment variables at the time of MCS initiation are composited
194 to minimize the confounding effects of MCS on the large-scale environment. MCS initiation is
195 defined as the first hour that an MCS cold cloud ($T_b$ < 241 K) is detected (Feng et al., 2018,
196 2019). All variables are normalized by removing their time mean and dividing by their standard
197 deviation over all MCS initiation times. A cosine latitude weighting is applied when the spatial
198 dimensions of the variables are collapsed into a single dimension.

To run SOM, the initiation nodes are assigned by randomly or more efficiently selecting them from the leading empirical orthogonal functions. Then we calculate the Euclidean distance between each input pattern and the initiation nodes to start an iterative procedure. The best-matching node or the "winning" node is the one with the shortest distance between the initiation nodes and the input pattern. Finally, the winning node and neighborhood nodes around the winner are updated to adjust themselves toward the input pattern. Since this process is iterated and fine-tuned by the inputs themselves, we call the nodes are self-organizing. The final SOM nodes are regarded as the large-scale environment types associated with MCSs. More details about the SOM analysis can be found from Song et al. (2019).

Here, we highlight the main differences from Song et al. (2019): (1) as the temporal resolution of the MCS track data and ERA5 reanalysis are both hourly, we can composite the environments at exactly the same time as the MCS initiation, but Song et al. (2019) had to reconcile the different temporal resolution between NARR (3-hourly) and the MCS track data (hourly); (2) Song et al. (2019) only adopted the fixed-space (Eulerian) compositing approach to focus on the large-scale environments, but here we also adopt the convection-centered (Lagrangian) compositing in addition to the fixed-space compositing to reveal the role of sub-synoptic perturbations in MCS initiation; (3) to conduct the composite analysis, Song et al. (2019) removed the seasonal mean, while here we first remove the 14-year averaged seasonal mean diurnal cycle to remove the impact of climatological diurnal cycle, followed by removing the five-day running mean to remove the impact of sub-seasonal variability. For example, August temperature is generally higher than that in June, so without removing the five-day running mean, MCSs that occur in August will be given more weighting on temperature and its

related fields, such as moisture. However, it is found that both methods show quite similar results in most fields analyzed here.

## 3. Results

### 3.1 Large-scale environments versus convection-centered environments

Analysis using SOM with respect to MCS initiation (purple box in Fig. 1a-d) reveals four types of summer MCS environments that differ substantially from one another in both the upper-level circulation and surface thermodynamic conditions at the synoptic scale (Fig. 1). At 200 hPa, the first two types (Type-1 and Type-2) feature anomalous cyclone to the west and anticyclone to the east of the MCS initiation (Fig. 1a-b). In contrast, the last two types (Type-3 and Type-4) show a reversed cyclone/anticyclone configuration, with anomalous anticyclone to the west and cyclone to the east of the MCS initiation (Fig. 1c-d). The differences between Type-1 and Type-2 are mainly the location and intensity of the anticyclone/cyclone: the intensity is much stronger in Type-1; Great Plains (shown as the purple box in Fig. 1a-d) is located between the anticyclone and cyclone in Type-1, while it is mainly located beneath the anticyclone in Type-2. Similar differences between Type-3 and Type-4 are also found. For example, the anticyclone in Type-4 is weak compared to the clear anticyclonic structure in Type-3. The upper-level anticyclone has a corresponding positive surface $\theta_e$ anomaly and the upper-level cyclone corresponds to a negative surface $\theta_e$ anomaly (shading in Fig. 1). The upper-level anticyclone/cyclone structure in the first two types favors the initiation of MCSs by cyclonic vorticity advection to the MCS initiation region, while the upper-level anticyclone/cyclone structure in the last two types suppresses the initiation of MCSs by anticyclonic vorticity advection to the MCS initiation region. Meanwhile, higher surface $\theta_e$ favors the initiation of

MCSs by destabilizing the local atmosphere, while lower surface $\theta_e$ suppresses the initiation of MCSs by stabilizing the local atmosphere. Hence, the large-scale environments are generally favorable for MCS initiation, especially in the warmer area of the Great Plains on the eastern side of the purple box in Type-1 and on the northern side in Type-2.

In Type-3, although the upper-level circulation seems unfavorable for MCS initiation, the wide-spread surface warmer $\theta_e$ supports MCS initiation. In Type-4, however, both upper-level large-scale circulation and surface $\theta_e$ do not support MCS initiation. Hence, sub-synoptic environments may play an important role in MCS initiation in Type-4. This speculation is supported by the convection-centered composites shown in Fig. 1e-h. It is clear that the convection-centered environments resemble the large-scale environments in the first three types, but this is not the case in Type-4. In Type-4, the convection-centered composite shows an upper-level cyclone to the west and anticyclone to the east of the MCS initiation location and a warmer surface $\theta_e$ around the location of MCS initiation, similar to Type-1 and Type-2 except for the much smaller spatial scale.

The GPLLJ and moisture transport are crucial in the MCS initiation. Here, we show the composites of 925 hPa wind and moisture anomalies in the four types in Fig. 2. Type-1 features a frontal structure, with southerly wind in the eastern Great Plains and northwesterly wind in the northwestern Great Plains. As a result, positive and negative moisture anomalies occur over the eastern and northwestern Great Plains, respectively (Fig. 2a). Both Type-2 and Type-3 feature enhanced low-level jet and positive moisture anomalies in the northern Great Plains (Fig. 2b-c). However, the enhanced jet and moisture anomalies occupy the whole northern Great Plains in Type-2, but they are confined to the northwestern Great Plains in Type-3. MCSs preferentially initiate in the vicinity of positive low-level moisture anomaly in the first three types. When it

266 comes to Type-4, the low-level wind anomalies are relatively weak and the Great Plains is
267 generally characterized by less moisture than normal, so the MCS initiation scatters around the
268 Great Plains and the Rocky Mountain foothills (Fig. 2d). In the convection-centered composites
269 of the low-level circulation and moisture, Type-4 is similar to all other types, with moisture
270 convergence and positive moisture anomalies around the storm initiation location (Fig. 2e-h).

271 The above large-scale environments composites based on the MCS tracking and hourly
272 ERA5 reanalysis datasets (Fig. 1a-d and Fig. 2a-d) resemble the large-scale environments
273 identified by Song et al. (2019) using 3-hourly NARR reanalysis, suggesting that the large-scale
274 environments associated with MCS initiation are robust and independent of the reanalysis
275 datasets. The convection-centered composites conducted here reveal some new features hidden
276 in the fixed-grid composites, especially for Type-3 that features an unfavorable large-scale
277 environment for MCS initiation at upper level and Type-4 that features an unfavorable large-
278 scale environment for MCS initiation at both upper level and surface. The smaller-scale cyclone
279 to the west and anticyclone to the east of MCS initiation (Fig. 1d) and the low-level moisture
280 convergence and high surface $\theta_e$ anomaly around the MCS initiation (Fig. 2h) indicate the role
281 played by sub-synoptic perturbations in Type-4.

282 The convection-centered environments are similar to the large-scale environments in the
283 first two types, but they differ substantially in Type-4, with the convection-centered
284 environments more supportive of MCS initiation than the large-scale environment. Hence, we
285 focus on the convection-centered composites in the following analysis. From a precursor
286 standpoint, it is critical to know whether the MCS initiation environments shown in Fig. 1e-h and
287 Fig. 2e-h precede the MCS initiation and thus trigger the MCSs. Figure 3 shows the convection-
288 centered environments at the same initiation location in four types except 12 hours before the

MCS initiation. The warm surface $\theta_e$ anomaly already occurs at the MCS initiation location even 12 hours before the MCS initiation, acting to destabilize the atmosphere (Fig. 3a-b). The upper-level cyclone/anticyclone are also already there. The low-level wind starts to converge around the initiation location and the moisture starts to increase 12 hours before the MCS initiation. It is also clear that all the anomalous environmental features are more westward displaced in all the four types (Fig. 3a-b vs. Fig. 1e-h; Fig. 3e-h vs. Fig. 2e-h) 12 hours earlier, indicating a possible eastward propagating feature.

### 3.2 Vertical structure of convection-centered environments

In order to further examine the MCS initiation environments, we show the vertical structure of convection-centered environments at the MCS initiation hour (0hr) and 12 hours earlier (-12hr). Temperature and moisture fields are first examined in Fig. 4. At 0hr, moisture anomalies maximize at the initiation location and larger moistening extends from the surface up to 400 hPa in all the four types (Fig. 4a-b). Interestingly, the warmest temperature anomaly occurs at the initiation location only in Type-3 and Type-4, but in Type-1 and Type-2, it occurs about 5° east of the initiation location. In Type-1 and Type-2, although the temperature anomaly at the initiation location is still positive, the magnitude is only about half of the temperature maximum. Type-1 features a typical deep front, with a cold anomaly to the west and a warm anomaly to the east of the initiation, but these are not that evident in Type-2. This is also consistent with what we see from the spatial distribution of the Type-1 environments (Fig. 2a). In Type-4, the warming is confined to the lower troposphere (below 700 hPa), but it can extend to the upper troposphere (250 hPa) in the other three types. This suggests that moisture is more important than temperature for the MCS initiation, no matter whether the large-scale environment is favorable or not. But importantly, when the large-scale environment is not

312 favorable (i.e., Type-3 and Type-4), the local temperature becomes more important in the MCS
313 initiation, with temperature anomalies also peaking at the initiation location. The temperature
314 anomaly at -12hr is very similar to that at 0hr, except with the westward shift. Compared to 0hr,
315 the moisture field at 12hr is also positive and displaced westward, but the anomaly is broader and
316 much smaller in magnitude (note the color scale difference). This suggests that both temperature
317 and moisture anomalies favorable for the MCS initiation already exist even 12 hours before the
318 MCS initiation and may propagate eastward gradually during the 12 hours. The moisture
319 anomalies become stronger and more concentrated at the MCS initiation location due to more
320 organized mesoscale convergence (Fig. 2e-h vs. Fig. 3e-h).

321 The vertical structure of the atmospheric circulation associated with the MCS initiation
322 is shown in Fig. 5. The upper-level cyclone/anticyclone structure shown in Fig. 1e-f is roughly
323 maintained in the whole free troposphere (above 700 hPa), i.e., a cyclone to the west and an
324 anticyclone to the east of the initiation location in Type-1, Type-2 and Type-4 and an anticyclone
325 at the initiation location in Type-3. Below 700 hPa, a cyclone anomaly occurs in all the four
326 types, corresponding to the boundary layer convergence anomalies. Correspondingly, a strong
327 and narrow upward motion anomaly occurs at the initiation location, which can extend up to 150
328 hPa. The cyclone and anticyclone anomaly at -12hr has similar magnitudes compared to the
329 anomaly at 0hr, but it is westward shifted. The upward motion occurs east of the cyclone and
330 west of the anticyclone and mostly west of the initiation location, with much weaker magnitude
331 and broader area. Hence, a clear eastward propagating feature of MCS initiation environments is
332 apparent at all vertical levels, which will be further discussed in the next subsection.

333 **3.3 Eastward propagating features of MCS initiation environments**

As mentioned above, MCS initiation environments appear much earlier than the initiation time and exhibit a gradual eastward propagation. This eastward propagating feature is more apparent in the longitude-time section plots of surface variables (Fig. 6) and upper-level/low-level variables (Fig. 7) along the latitude of MCS initiation. Precipitation increases rapidly after the MCS initiation and propagates eastward in all four types (cyan contour in Fig. 6). This reflects the propagating nature of MCSs (e.g., Carbone et al., 2002). All other variables related to MCS initiation also exhibit clear eastward propagation and precede the MCS initiation in all four types of large-scale environments, including the lower surface pressure and higher surface $\theta_e$ (Fig. 6), anomalous cyclone and higher PV to the west and anomalous anticyclone and lower PV to the east of MCS initiation location (Fig. 7a-d), as well as positive low-level moisture anomaly (Fig. 7e-h) in an eastward-propagating and preceding fashion with respect to the MCS initiation. Note that after the MCS initiation, stronger and faster propagating PV signals are apparent (darker blue streaks in Fig. 7a-d). This propagating feature is likely related to PV generation associated with the stratiform region and top-heavy latent heating profile of MCSs that contribute to the longer lifetime of MCSs relative to isolated deep convection (Raymond and Jiang 1990; Yang et al., 2017; Feng et al., 2018). The clear differences between the PV that exists before MCS initiation and the more dominant and faster propagating PV with shorter wavelength after MCS initiation underscore the role of the precursor eastward propagating feature in summer MCS initiation in the Great Plains and its distinction from the PV generation due to MCS rainfall.

Except for the low-level moisture, the propagating environments shown in Fig. 6 and Fig. 7 can be traced back 36 hours to 10°-15° west of the MCS initiation in Type-1 and Type-2, 18 hours to around 10° west of the MCS initiation in Type-3 and 36 hours to ~15° west of the MCS

357 initiation in Type-4. The frontal feature is most evident in Type-1, with cold $\theta_e$ comparable to the
358 warm $\theta_e$ starting from ~30 hours before the MCS initiation. In the other types, the cold $\theta_e$
359 anomaly is much smaller than the warm $\theta_e$ anomaly. The surface pressure anomaly and gradient
360 in Type-1 and Type-2 is much stronger than the other two types, supporting that the synoptic-
361 scale forcing is stronger for the first two types. The low-level moisture anomalies seem to be
362 more localized as they develop only 12 hours earlier, up to 10° west of MCS initiation, more
363 evidently in Type-3 and Type-4. This is expected considering the main source of low-level
364 moisture is confined to the Great Plains by the Rocky Mountains to the west. At the upper level,
365 the environments are modified considerably after the MCS initiation (Fig. 7a-d), possibly due to
366 the top-heavy diabatic heating from the increased stratiform precipitation associated with mature
367 MCSs, consistent with previous studies (Yang et al., 2017; Feng et al., 2018).

368 Given that the convection-centered composites shown in Fig. 7 are associated with MCS
369 initiation spanning a longitudinal range of 15° from the foothill of the Rocky Mountains to the
370 central Great Plains, the precursor environments 10°-15° west of the convection centers (Fig. 7)
371 could be co-located with the Rocky Mountains or further upstream. To better understand the role
372 of the Rocky Mountains and regions further upstream in producing the precursor environments
373 of MCS initiation found in this study, we isolate the MCS initiation at the foothill of the Rocky
374 Mountains (35°-50°N, 100°-105°W) and plot the longitude-time composite of upper-level and
375 low-level environments along the latitude of MCS initiation (Fig. 8). The composite for MCS
376 initiation at the foothill (Fig. 8a-d) and that for MCS initiation across a wider range of longitudes
377 (Fig. 7a-d) show similar upper-level feature, suggesting that the propagating environments such
378 as upper-level short wave exist further upstream than the Rocky Mountains (Tuttle & Davis,
379 2013). However, the surface moisture composite of MCS initiation confining to the foothill

suggests that the low-level moisture only starts to accumulate shortly before the MCS initiation and has no propagating feature, as is evident in Type-1 and Type-3 (Fig. 5e-h). This is mainly because their sources of moisture are different: for MCS initiation at the foothill, moisture is largely local while for MCS initiation over the central Great Plains (east of 100°W), moisture propagates along with other dynamical environments. But at the foothill, there is not enough moisture upstream to respond to the propagating waves. Hence, it is expected that the MCSs initiated at the plains can produce more rainfall than those initiated at the foothill due to more abundant moisture supply. This is indeed the case, as composite precipitation from MCSs initiated at the Great Plains among all four types of large-scale environments is consistently higher than those initiated at the foothills, particularly within the first 6 hours after initiation when foothill initiated MCSs have not propagated too far away from the Rocky Mountains yet (Fig. S1). These results suggest that local low-level moisture combined with a traveling wave is key to the initiation of MCSs at the foothill, but over the central Great Plains (east of 100°W), it is the coupling of the dynamical and moisture anomalies associated with eastward propagating waves that supports MCS initiation.

### 3.4 The role of MPs in the MCS initiation

To examine the role of MPs in the MCS initiation east of the Rocky Mountains, we utilize two datasets from independent MP tracking and MCS tracking to determine the likelihood of co-occurrence of MPs and MCS initiation. To do this, we check whether there is an active MP that spatially overlaps with the MCS cloud mask at the time of an MCS initiation. If so, we consider this MCS initiation to be associated with or influenced by an MP. Based on the convection-centered composites, the 600 hPa positive relative vorticity is located slightly west of the center of MCS initiation (Wang et al., 2009). Accounting for this spatial relationship, an

403 active MP (initiated before this moment) found within 5° west of the MCS cloud mask at the
404 time of the MCS initiation is counted as a co-occurrence of MPs and MCS initiation.

405 Figure 9 provides more details of the calculation and the results are shown in Table 1.
406 Over the 14 years (2004-2017) analyzed, most of the MCS initiations associated with MPs occur
407 under Type-4 (over 60%), consistent with our expectation that sub-synoptic perturbations play a
408 more important role in MCS initiation in Type-4 with the weakest large-scale forcing. These 55
409 MCS initiations associated with MPs only account for less than 5% of the total MCS initiation in
410 this period (1135 MCSs in total). But considering only the 189 MPs in the 14 years, nearly 30%
411 of MPs are associated with MCS initiation. The considerable number of MPs associated with
412 MCS initiation suggests that MPs may provide a source of predictability for the Type-4 MCSs
413 (Wang et al. 2009). We next examine whether the MCSs associated with MPs are different from
414 those without MPs. We compare the probability distribution function of MCS rainfall amount,
415 rainfall area, mean rain rate and the 40 dBZ convective echo-top height between MCSs with and
416 without MPs (Fig. 10). Compared to MCSs without MPs, MCSs with MPs show lower
417 probability at low rainfall amounts/areas/rates and echo-top heights, but higher probability on the
418 high ends of rainfall amount (mainly from the stratiform rainfall amount), rainfall area (both
419 from convective and stratiform rainfall area), mean rain rate (mainly from convective rain rate)
420 and echo-top height. This suggests that MPs have a distinctively larger chance to invigorate
421 MCSs by producing more extreme rainfall over a larger area with a stronger convective activity
422 (i.e., strong winds and hail), under the weak synoptic-scale forcing associated with Type-4 MCS
423 environments.

424 **4. Conclusion and discussion**

In this study, self-organizing map analysis is conducted to identify four typical types of propagating MCS initiation environments to better quantify the environments at the time of MCS initiation, based on an MCS tracking database and the latest ERA5 reanalysis, providing data at higher temporal resolution than those previously used in Song et al. (2019). We also examine the relative roles of the large-scale and sub-synoptic environments in the MCS initiation for each type of environments identified by the SOM analysis. These analyses highlight the crucial role of propagating sub-synoptic perturbations in the MCS initiation during summer. Moreover, we quantify the role of MPs in the MCS initiation over the Great Plains under unfavorable large-scale environment for MCSs. The main conclusions are summarized as follows:

(1) The four types of MCSs identified by SOM analysis differ substantially in terms of the large-scale environments. The first two types feature large-scale favorable environments in the whole troposphere and surface; the large-scale environment is unfavorable at the upper-level in Type-3 but favorable at the low-level and surface. The large-scale environments in Type-4 with negative vorticity advection and less moisture transport are most unfavorable for MCS initiation. To investigate sub-synoptic factors supporting MCS initiation, we also analyze convection-centered composites. The large-scale environments and convection-centered environments are similar for the first three types, but they are distinct in Type-4. While Type-4 also features an upper-level cyclone to the west and an anticyclone to the east of MCS initiation and higher $\theta_e$ near the surface similar to the features of the first two types, its circulation spatial scale is much smaller. These results suggest that the MCS initiation in Type-4 is supported by dynamical and thermodynamic processes similar to those of the other three types, but these processes are associated with sub-synoptic perturbations instead of large-scale forcing.

(2) The convection-centered composites clearly show the dominance of eastward propagating features prior to MCS initiation in all four types of MCS initiation environments. These propagating features are clear at all vertical levels and appear much earlier (up to 36 hours) before the MCS initiation. Such precursors may provide some potential predictability for summertime MCSs over the Great Plains. Some of the propagating perturbations originate from the Rocky Mountains, while others can be traced back further west to the Pacific Northwest. Both propagating environments and local, non-propagating low-level moisture are found to be important in MCS initiation at the foothill of the Rocky Mountains, while in the Great Plains, MCS initiation is supported by the coupled dynamical and thermodynamic propagating features. Hence, the MCSs initiated at the plains can produce more rainfall than those initiated at the foothill due to more abundant moisture supply.

(3) The role of MPs, a type of sub-synoptic perturbations under anticyclonic upper-level circulation, in MCS initiation is revealed. Although less than 5% of MCS initiations are related to MPs, 30% of MPs are related to MCS initiation (MPs occur much less frequently than MCSs: 189 vs. 1135 for 2004-2017 summer). The association of MPs with MCSs is most frequently observed in Type-4 MCSs (over 60%), consistent with the understanding that under unfavorable large-scale environments, sub-synoptic perturbations play a more important role in MCS initiation in Type-4 than the other three types. Although MPs are only responsible for a small fraction of MCS initiation, the associated Type-4 MCSs have a higher probability of producing more rainfall amount, larger MCS rainfall areas, and more intense convection and rain rate than those that are not associated with MPs.

Previous studies have identified different kinds of summer MCS initiation environments both at large scale and smaller scale (e.g., Maddox, 1983; Anderson & Arritt 1998; Laing &

Fritsch, 2000; Coniglio et al. 2004, 2010; Peters & Schumacher, 2014; Yang et al. 2017; Song et al. 2019). Eastward propagating environments have also been found by many previous studies to be associated with rainfall over the Great Plains (e.g., Li & Smith 2010; Wang et al. 2011a, b; Tuttle & Davis 2013; Pokharel et al., 2019). However both MCS and non-MCS storms contribute similar amount of rainfall in the Great Plains so it is unclear whether and how the eastward propagating environments may play a role in the summer MCS initiation. Taking advantage of high spatiotemporal datasets that have only become available recently, this study has filled the gap in understanding the environments for summer MCS initiation by identifying the crucial role of eastward propagating environments. Further, we have quantified the contribution from a specific kind of propagating environments, namely mid-tropospheric perturbations. Future studies should examine contributions from other kinds of propagating environments, such as shortwaves (Tuttle & Davis 2013) to the summer MCS initiation.

This study also shows that local, non-propagating low-level moisture anomaly is also important for MCS initiation at the foothill of Rocky Mountains, but the limited spatiotemporal scale may present a challenge for prediction. While such anomaly is likely related to the GPLLJ moisture transport, the role of soil moisture also deserves some attention as the study region is known to be a hot spot of land-atmosphere interactions (Koster et al., 2004). Remote sensing of soil moisture offers a significant opportunity to advance understanding of the role of soil moisture in MCS development (Klein & Taylor, 2020). Convection-permitting models are also useful tools for studying MCSs. For example, we can examine whether the frequency of large-scale favorable environments for MCS initiation in convection-permitting models is comparable with observations, as Feng et al. (2021) noted that the frequency of large-scale favorable environments is significantly underestimated in a high-resolution climate model (25-km) with

493 convection parameterization, contributing to the underestimated frequency of MCSs. As
494 convection-permitting models also need improvements in the simulation of MCSs during
495 summer compared to spring (e.g., Prein et al., 2020), an interesting question arises as to whether
496 they suffer in producing the sub-synoptic perturbations for summer MCS initiation under weak
497 large-scale environment and/or the local moisture anomaly found in this study. Advancing both
498 understanding and modeling of the precursors of MCSs and associated forcing and mechanisms
499 is important for realizing the potential of the precursors for improving prediction of summertime
500 MCSs that have significant impacts on the surface water balance (Hu et al., 2020).

**Acknowledgement**

This research is supported by the U.S. Department of Energy Office of Science Biological and Environmental Research as part of the Regional and Global Climate Modeling program area. PNNL is operated for the Department of Energy by Battelle Memorial Institute under contract DE-AC05-76RL01830. The MCS database over the U.S. is obtained from the Department of Energy Atmospheric Radiation Program (ARM): https://doi.org/10.5439/1571643, and the ERA5 dataset is obtained at https://cds.climate.copernicus.eu/#!/search?text=ERA5&type=dataset.

508 **References**

509 Anderson, C. J., & Arritt, R. W., (1998). Mesoscale convective complexes and persistent
510 elongated convective systems over the United States during 1992 and 1993. *Mon. Wea.*
511 *Rev.*, 126, 578–599.

512 Carbone, R. E., Tuttle, J. D., Ahijevych, D. A., & Trier, S. B., (2002). Inferences of
513 Predictability Associated with Warm Season Precipitation Episodes. *J. Atmos. Sci.*, 59, 2033–
514 2056.

515 Coniglio, M. C., Stensrud, D. J., & Richman, M. B., (2004). An observational study of derecho-
516 producing convective systems. *Wea. Forecasting*, 19, 320–337.

517 Coniglio, M. C., Hwang, J. Y., & Stensrud, D. J., (2010). Environmental factors in the upscale
518 growth and longevity of MCSs derived from rapid update cycle analyses. *Monthly Weather*
519 *Review*, 138, 3514–3539. https://doi.org/10.1175/2010MWR3233.1; Corrigendum, 139, 2686–
520 2688, doi:10.1175/MWR−D−11−00064.1

521 Cooney, J. W., Bowman, K. P., Homeyer, C. R., & Fenske, T. M., (2018). Ten-year analysis of
522 tropopause-overshooting convection using GridRad data, *J. Geophys. Res.*, 123, 329–343, doi:
523 10.1002/2017JD0277181.

524 Davis, C. A., Ahijevych, D. A., & Trier, S. B. (2002). Detection and Prediction of Warm Season
525 Midtropospheric Vortices by the Rapid Update Cycle, *Monthly Weather Review*, 130(1), 24-42.

526 Feng, Z. et al., (2016). More frequent intense and long-lived storms dominate the springtime
527 trend in central US rainfall. *Nat. Commun.* 7, 13429, doi:10.1038/ncomms13429.

528 Feng, Z., Leung, L. R., Houze, R. A., Hagos, S., Hardin, J., Yang, Q., Han, B., & Fan, J., (2018).
529 Structure and evolution of mesoscale convective systems: Sensitivity to cloud microphysics in

530 convection-permitting simulations over the United States. *J. Adv. Model. Earth Syst*., 10, 1470–
531 1494.

532 Feng, Z., Houze, R. A., Leung, L. R., Song, F., Hardin, J. C., Wang, J., Gustafson, W. I., &
533 Homeyer, C. R., (2019). Spatiotemporal Characteristics and Large-Scale Environments of
534 Mesoscale Convective Systems East of the Rocky Mountains. *J. Climate*, 32, 7303–7328.

535 Feng, Z., (2019). Mesoscale convective system (MCS) database over United States, V2.
536 Atmospheric Radiation Measurement Program, accessed 1 January 2020,
537 https://doi.org/10.5439/1571643.

538 Feng, Z., Song, F., Sakaguchi, K., & Leung, L. R., (2021). Evaluation of Mesoscale Convective
539 Systems in Climate Simulations: Methodological Development and Results from MPAS-CAM
540 over the U.S.. *J. Climate*, 34(7), 2611-2633.

541 Gao, Y., Leung, L. R., Zhao, C., & Hagos, S., (2017). Sensitivity of summer precipitation to
542 model resolution and convective parameterizations across gray zone resolutions. *J. Geophys.*
543 *Res*., 122, 2714-2733, doi:10.1002/2016JD025896.

544 Haberlie, A. M. & Ashley, W. S., (2019). A radar-based climatology of mesoscale convective
545 systems in the United States. *J. Climate*, 32, 1591–1606.

546 Hersbach, H., et al., (2020). The ERA5 global reanalysis. Quart. J. Roy. Meteor. Soc.,
547 https://doi.org/10.1002/qj.3803.

548 Homeyer, C. R., & Bowman, K. P., (2017). Algorithm Description Document for Version 3.1 of
549 the Three-Dimensional Gridded NEXRAD WSR-88D Radar (GridRad) Dataset, Technical
550 Report.

551 Houze, R. A., (2004). Mesoscale convective systems. *Reviews of Geophysics*, 42, RG4003.

552 Houze, R. A., (2018). 100 Years of research on mesoscale convective systems. *Meteorological*
553 *Monographs*, **59**, 17.1–17.54, https://doi.org/10.1175/AMSMONOGRAPHS-D-18-0001.1.

554 Hu, H., Leung, L. R., & Feng, Z., (2020). Understanding the distinct impacts of MCS and non-
555 MCS rainfall on the surface water balance in the central U.S. using a numerical water-tagging
556 technique. *J. Hydrometeor*., doi:10.1175/JHM-D-20-0081.1.

557 Huang, X., Hu, C., Huang, X. et al. A long-term tropical mesoscale convective systems dataset
558 based on a novel objective automatic tracking algorithm. Clim Dyn 51, 3145–3159 (2018).
559 https://doi.org/10.1007/s00382-018-4071-0.

560 Janowiak, J., Joyce, B., & Xie, P., (2017). NCEP/CPC L3 Half Hourly 4km Global (60S - 60N)
561 Merged IR V1, edited by Andrey Savtchenko, Greenbelt, MD, Goddard Earth Sciences Data and
562 Information Services Center (GES DISC), Accessed: ***[1 February***
563 ***2018]***, 10.5067/P4HZB9N27EKU.

564 Johns, R. H., (1982). A synoptic climatology of northwest flow severe weather outbreaks. Part I:
565 nature and significance. *Mon. Weather Rev.*, 110, 1653–1663.

566 Johns, R. H., (1984). A synoptic climatology of northwest flow severe weather outbreaks. Part II:
567 meteorological parameters and synoptic patterns. *Mon. Weather Rev.*, 112, 449–464.

568 Johns R. H., (1993). Meteorological conditions associated with bow echo development in
569 convective storms. *Weather Forecast*, 8, 294–299.

570 Koster, R.D., et al., (2004). Regions of strong coupling between soil moisture and precipitation.
571 *Science*, 305, 1138, doi:10.1126/science.1100217.

572 Klein, C., & Taylor, C. M., (2020). Dry soils can intensify mesoscale convective systems. *Proc.*
573 *Nat. Acad. Sci*., 117 (35), 21132-21137, doi:10/1073/pnas.2007998117.

574 Laing, A. G. & Fritsch, J. M., (2000). The large scale environments of the global populations of
575 mesoscale convective complexes. *Mon. Weather Rev.* 128, 2756–2776.

576 Li, Y., & Smith, R. B., (2010). The detection and significance of diurnal pressure and potential
577 vorticity anomalies east of the Rockies. J. *Atmos. Sci.*, 67, 2734–2751.

578 Lin, Y., (2011). GCIP/EOP Surface: Precipitation NCEP/EMC 4KM Gridded Data (GRIB) Stage
579 IV Data. Version 1.0. UCAR/NCAR - Earth Observing Laboratory.
580 https://doi.org/10.5065/D6PG1QDD. Accessed Nov 2017.

581 Lin, Y., Dong, W., Zhang, M., Xie, Y., Xue, W., Huang, J., & Luo, Y. (2017). Causes of model
582 dry and warm bias over central U.S. and impact on climate projections. *Nature Communications*,
583 8(1), 881. https://doi.org/10.1038/s41467-017-01040-2.

584 Ma, H.-Y., Klein, S. A., Xie, S., Zhang, C., Tang, S., Tang, Q., et al., (2018). CAUSES: On the
585 Role of Surface Energy Budget Errors to the Warm Surface Air Temperature Error Over the
586 Central United States. *Journal of Geophysical Research: Atmospheres*, 123(5), 2888-2909.
587 https://agupubs.onlinelibrary.wiley.com/doi/abs/10.1002/2017JD027194.

588 Maddox, R. A., Chappell, C. F., & Hoxit, L. R., (1979). Synoptic and meso-α-scale aspects of
589 flash flood events. *Bull. Amer. Meteor. Soc.*, 60, 115–123, doi:10.1175/1520-0477-60.2.115.

590 Maddox, R. A., (1983). Large-scale meteorological conditions associated with midlatitude,
591 mesoscale convective complexes. *Monthly Weather Review*, 111(7), 1475–1493.

592 Mesinger, F., and Coauthors, (2006). North American Regional Reanalysis. *Bulletin of the*
593 *American Meteorological Society*, **87,** 343-360.

Peters, J. M., & Schumacher, R. S., (2014). Objective categorization of heavy-rain-producing MCS synoptic types by rotated principal component analysis. *Monthly Weather Review*, 142(5), 1716-1737.

Pokharel, B., Wang, S. Y., Meyer, J., Gillies, R., & Lin, Y., (2019). Climate of the weakly-forced yet high-impact convective storms throughout the Ohio River Valley and Mid-Atlantic United States. *Clim. Dyn.*, 52, 5709–5721.

Prein, A.F., Liu, C., Ikeda, K., et al., (2020). Simulating North American mesoscale convective systems with a convection-permitting climate model. *Clim. Dyn.*, 55, 95–110. https://doi.org/10.1007/s00382-017-3993-2

Raymond, D. J., & Jiang, H., (1990). A theory for long-lived mesoscale convective systems. *J. Atmos. Sci*., 47(24), 3067-3077.

Schumacher, R. S., & Johnson, R. H., (2005). Organization and environmental properties of extreme-rain-producing mesoscale convective systems. *Mon. Wea. Rev.*, 133, 961–976.

Schumacher, R. S., & Johnson, R. H., (2006). Characteristics of U.S. extreme rain events during 1999–2003. *Wea. Forecasting*, 21, 69–85.

Stein, T. H. M., Hogan, R. J., Hanley, K. E., Nicol, J. C., Lean, H. W., Plant, R. S., Clark, P. A., & Halliwell, C. E. (2014). The Three-Dimensional Morphology of Simulated and Observed Convective Storms over Southern England, *Monthly Weather Review*, 142(9), 3264-3283.

Trier, S. B., Davis, C. A., Ahijevych, D. A., Weisman, M. L., & Bryan, G. H., (2006). Mechanisms Supporting Long-Lived Episodes of Propagating Nocturnal Convection within a 7-Day WRF Model Simulation. *J. Atmos. Sci.*, 63, 2437–2461.

615 Tuttle, J. D., & Davis, C. A., (2013). Modulation of the Diurnal Cycle of Warm-Season
616 Precipitation by Short-Wave Troughs. *J. Atmos. Sci.*, 70, 1710–1726.

617 Wang, S., Chen, T., & Taylor, S. E., (2009). Evaluations of NAM Forecasts on Midtropospheric
618 Perturbation-Induced Convective Storms over the U.S. Northern Plains. *Wea. Forecasting*, 24,
619 1309–1333, https://doi.org/10.1175/2009WAF2222185.1.

620 Wang, S., Chen, T. C., & Correia, J., (2011a). Climatology of summer midtropospheric
621 perturbations in the US northern plains. Part I: Influence on northwest flow severe weather
622 outbreaks. *Clim. Dyn.*, 36, 793–810.

623 Wang S., Chen, T. C., & Takle, E. S., (2011b). Climatology of summer midtropospheric
624 perturbations in the US northern plains. Part II: Large-scale effects of the Rocky Mountains on
625 genesis. *Clim. Dyn.*, 36,1221–1237.

626 Yang, Q., Houze, R. A., Leung, L. R., & Feng, Z., (2017). Environments of long-lived mesoscale
627 convective systems over the central United States in convection permitting climate
628 simulations. *J. Geophys. Res. Atmos.*, 122, 13 288–13 307.

629 **Table captions**

630 **Table 1** The MCS number in each type, total MP number and the number of overlaps between
631 MCS and MP in each type for 2004-2017 summer (June-July-August). The percentage of
632 overlaps to the total MCS number in each type is also shown in the bracket.

633 **Figure captions**

634 **Fig. 1** (a-d) Composite anomalies of 200 hPa geopotential height (contour; units: m) and surface
635 equivalent potential temperature (shading; units: K) during June-July-August (JJA) in each type
636 of large-scale environment determined by the SOM analysis. The anomalies are relative to all
637 times during JJA. The percentage in the upper right corner indicates the percentage of occurrence
638 of each environment type. The solid (dashed) lines represent positive (negative) 200 hPa
639 geopotential height anomalies, with an interval of 5 m. (e-h) The same as (a-d) but for
640 convection-centered composites. The purple and black boxes in (a-d) indicate the boundaries of
641 MCS initiation over the Great Plains (25°-50°N, 90°-105°W) and the SOM analysis domain (20°
642 -55°N, 70°-110°W), respectively. The cyan dots denote the location of MCS initiation. The
643 purple dot in (e-h) indicates the MCS initiation location (0°, 0°); E (W) in the x-axis means east
644 (west) of the convection initiation and N (S) in the -axis means north (south) of the convection
645 initiation.

646 **Fig. 2** Same as Fig. 1 but for 925 hPa wind (vector; units: m $s^{-1}$) and specific humidity (shading;
647 units: g $kg^{-1}$). The grey contour in (a-d) shows elevation higher than 1500 m based on the
648 TBASE data.

649 **Fig. 3** The convection-centered composite anomalies of (top panel) 200 hPa geopotential height
650 (contour; units: m) and surface equivalent potential temperature (shading; units: K), and (bottom
651 panel) 925 hPa wind (vector; units: m $s^{-1}$) and specific humidity (shading; units: g $kg^{-1}$) at the 12
652 hours before the MCS initiation during June-July-August (JJA) in each type of large-scale
653 environment determined by the SOM analysis. The purple dot indicates the MCS initiation
654 location (0°, 0°); E (W) in the x-axis means east (west) of the convection initiation and N (S) in
655 the y-axis means north (south) of the convection initiation.

**Fig. 4** Longitude-height cross-sections of specific humidity (shading; units: g $kg^{-1}$) and temperature (contour; units: K) in the convection-centered composites in the four types at the initiation hour (top panel) and 12 hours before the initiation (bottom panel). Purple line shows the initiation location. E (W) in the x-axis means east (west) of the convection initiation. The contour interval is 0.3 K and the bold line is the zero contour.

**Fig. 5** Same as Fig. 4 but for vertical velocity (shading; units: $10^{-2}$ Pa $s^{-1}$) and geopotential height (contour; units: m). The contour interval is 3 m.

**Fig. 6** The longitude-time section of convection-centered environments along the latitude of MCS initiation spanning from the foothill of the Rocky Mountains to the central Great Plains (25 °-50°N, 90°-105°W; purple boxes in Fig.1a-d and Fig. 2a-d): surface equivalent potential temperature (shading; units: K), surface pressure (black contour; units: hPa) and precipitation (cyan contour; units: mm $day^{-1}$). The black solid (dashed) lines represent positive (negative) surface pressure, with an interval of 0.3 hPa. The solid cyan lines represent positive precipitation, with an interval of 0.3 mm/day. The purple dot indicates the MCS initiation longitude and moment (0° and 0 hr); E (W) in the x-axis means east (west) of the convection initiation and + (-) in the y-axis means after (before) the convection initiation.

**Fig. 7** The longitude-time section of convection-centered environments along the latitude of MCS initiation spanning from the foothill of the Rocky Mountains to the central Great Plains (25 °-50°N, 90°-105°W; purple boxes in Fig.1a-d and Fig. 2a-d): (a-d) 200 hPa potential vorticity (shading; units: $10^{-6}$ K $m^2$ $kg^{-1}$ $s^{-1}$) and geopotential height (contour: units: m) and (e-h) 925 hPa specific humidity (units: g $kg^{-1}$). In (a-d), the black solid (dashed) lines represent positive (negative) geopotential height, with an interval of 3 m. The purple dot indicates the MCS

678 initiation longitude and moment (0° and 0 hr); E (W) in the x-axis means east (west) of the
679 convection initiation and + (-) in the y-axis means after (before) the convection initiation.

680 **Fig. 8** Same as Fig. 4 but for MCSs initiated at the foothill of Rocky Mountain (35°-50°N; 100°-
681 105°W).

682 **Fig. 9** Schematic plot of the calculation of overlap between mid-tropospheric perturbation (MP)
683 and MCS based on their respective tracking records. The different colors in this map show the
684 different numbers assigned to each MCS at initiation (shown as cloud numbers). The highest
685 number of 281 is for MCSs initiated at the presented time (2009-07-30-Z01). At the moment of
686 MCS initiation, we search the MP tracking record for a spatial overlap between the new MCS
687 and an active MP (the MP should be initiated before this moment). The spatial extent of each MP
688 is represented by the blue square based on the center coordinate and areal coverage (in terms of
689 the number of the ERA5 grid points) provided by the MP tracking algorithm (circular shape is
690 also tested and gives the same results). As the MP has a threshold and the grid points with lower
691 values are not labeled as MP, the MP area coverage is doubled (we also tested even larger area,
692 but the results are unchanged) to consider the potential impacts of these lower values on the
693 MCS initiation.

694 **Fig. 10** Probability distribution function (PDF) of (a) MCS rainfall amount (units: $10^4$ mm $hr^{-1}$),
695 (b) MCS rainfall area (units: $10^4$ $km^2$), (c) MCS rain rate (units: mm $hr^{-1}$) and (d) 40 dBZ echo
696 top height (units: km) in Type-4 with (blue bar) and without (red bar) MPs.

**Table 1** The MCS number in each type of large-scale environments, the total MP number and the number of overlaps between MCS initiations and MPs in each type for 2004-2017 summer (June-July-August). The percentage of overlaps in the total MCS number in each type is also shown in the bracket.

| | **Type-1** | **Type-2** | **Type-3** | **Type-4** |
|---|---|---|---|---|
| **MCS number** | 336 | 235 | 217 | 347 |
| **MP number** | 189 | | | |
| **MCS overlap with MP** | 9 (2.7%) | 7 (3.0%) | 5 (2.3%) | 34 (10%) |

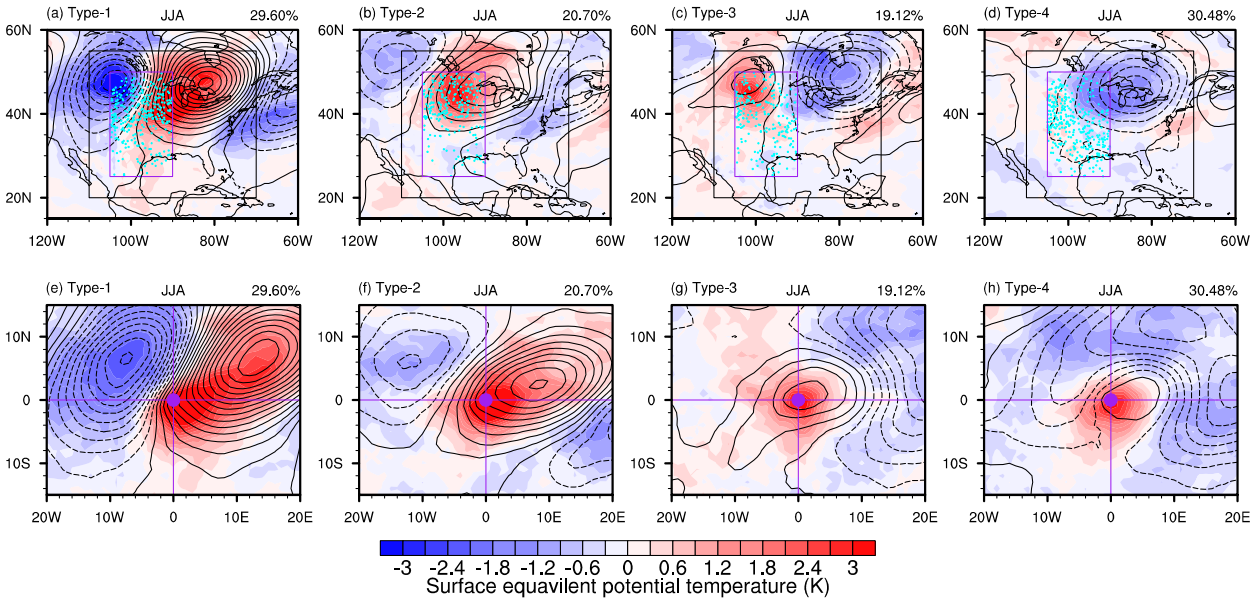


**Fig. 1** (a-d) Composite anomalies of 200 hPa geopotential height (contour; units: m) and surface equivalent potential temperature (shading; units: K) during June-July-August (JJA) in each type of large-scale environment determined by the SOM analysis. The anomalies are relative to all times during JJA. The percentage in the upper right corner indicates the percentage of occurrence of each environment type. The solid (dashed) lines represent positive (negative) 200 hPa geopotential height anomalies, with an interval of 5 m. (e-h) The same as (a-d) but for convection-centered composites. The purple and black boxes in (a-d) indicate the boundaries of MCS initiation over the Great Plains (25°-50°N, 90°-105°W) and the SOM analysis domain (20° -55°N, 70°-110°W), respectively. The cyan dots denote the location of MCS initiation. The purple dot in (e-h) indicates the MCS initiation location (0°, 0°); E (W) in the x-axis means east (west) of the convection initiation and N (S) in the -axis means north (south) of the convection initiation.

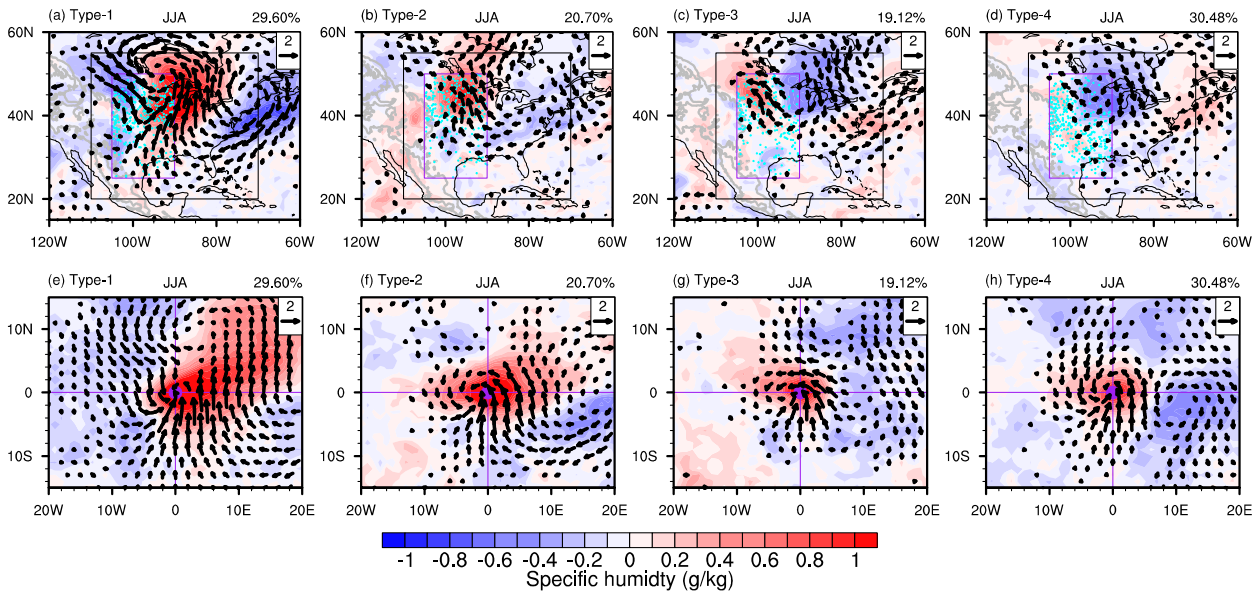


715

716 **Fig. 2** Same as Fig. 1 but for 925 hPa wind (vector; units: m $s^{-1}$) and specific humidity (shading;
717 units: g $kg^{-1}$). The grey contour in (a-d) shows elevation higher than 1500 m based on the
718 TBASE data. The vector with wind speed smaller than 0.2 m $s^{-1}$ is omitted.

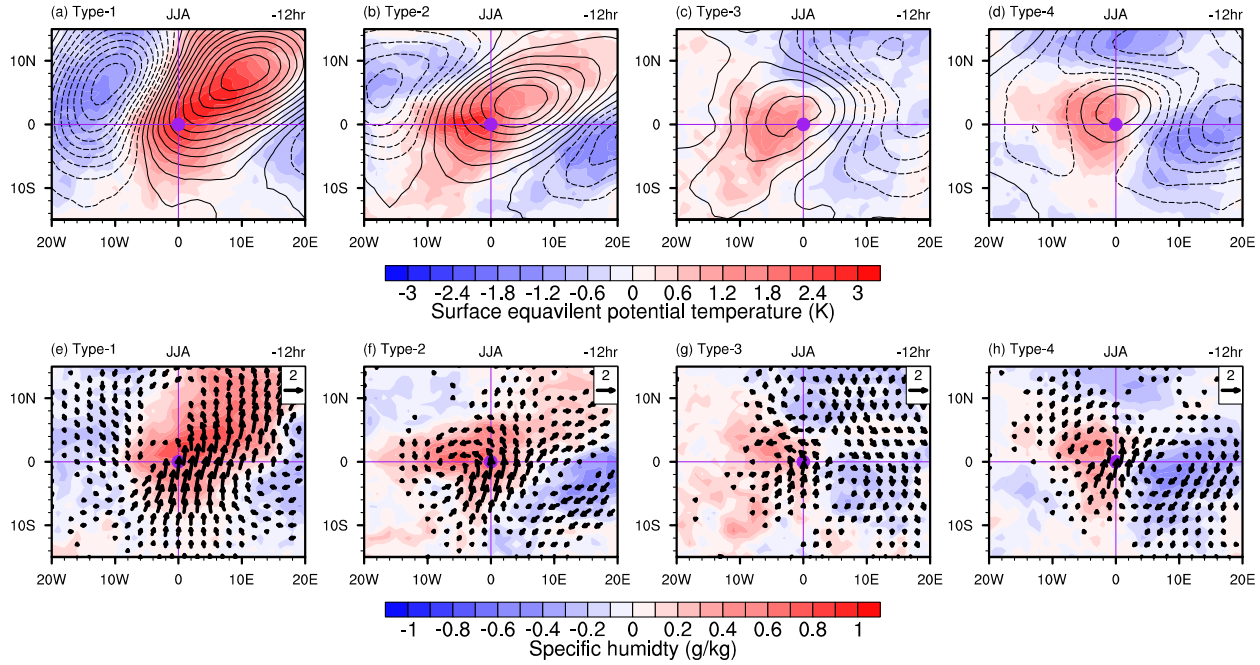


719

720 **Fig. 3** The convection-centered composite anomalies of (top panel) 200 hPa geopotential height
721 (contour; units: m) and surface equivalent potential temperature (shading; units: K), and (bottom
722 panel) 925 hPa wind (vector; units: m $s^{-1}$) and specific humidity (shading; units: g $kg^{-1}$) at the 12
723 hours before the MCS initiation during June-July-August (JJA) in each type of large-scale
724 environment determined by the SOM analysis. The purple dot indicates the MCS initiation
725 location (0°, 0°); E (W) in the x-axis means east (west) of the convection initiation and N (S) in
726 the y-axis means north (south) of the convection initiation. The vector with wind speed smaller
727 than 0.2 m $s^{-1}$ is omitted.

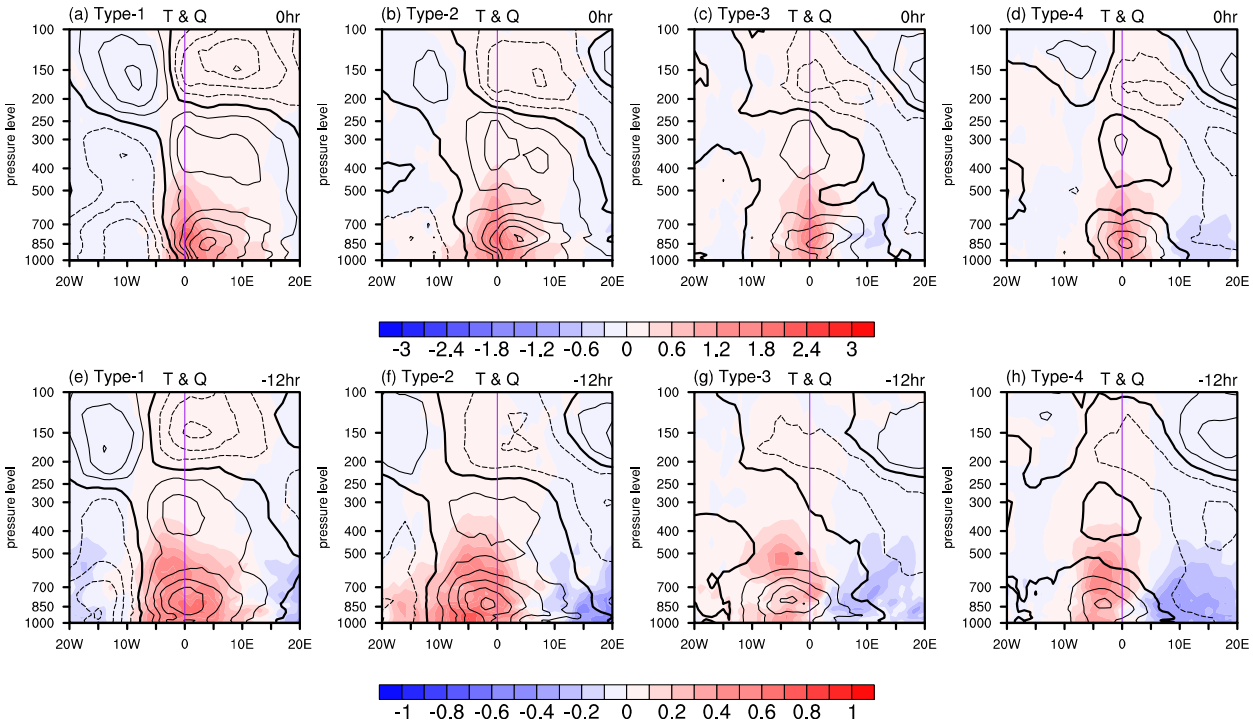


728

729 **Fig. 4** Longitude-height cross-sections of specific humidity (shading; units: g $kg^{-1}$) and
730 temperature (contour; units: K) in the convection-centered composites in the four types at the
731 initiation hour (top panel) and 12 hours before the initiation (bottom panel). Purple line shows
732 the initiation location. E (W) in the x-axis means east (west) of the convection initiation. The
733 contour interval is 0.3 K and the bold line is the zero contour.

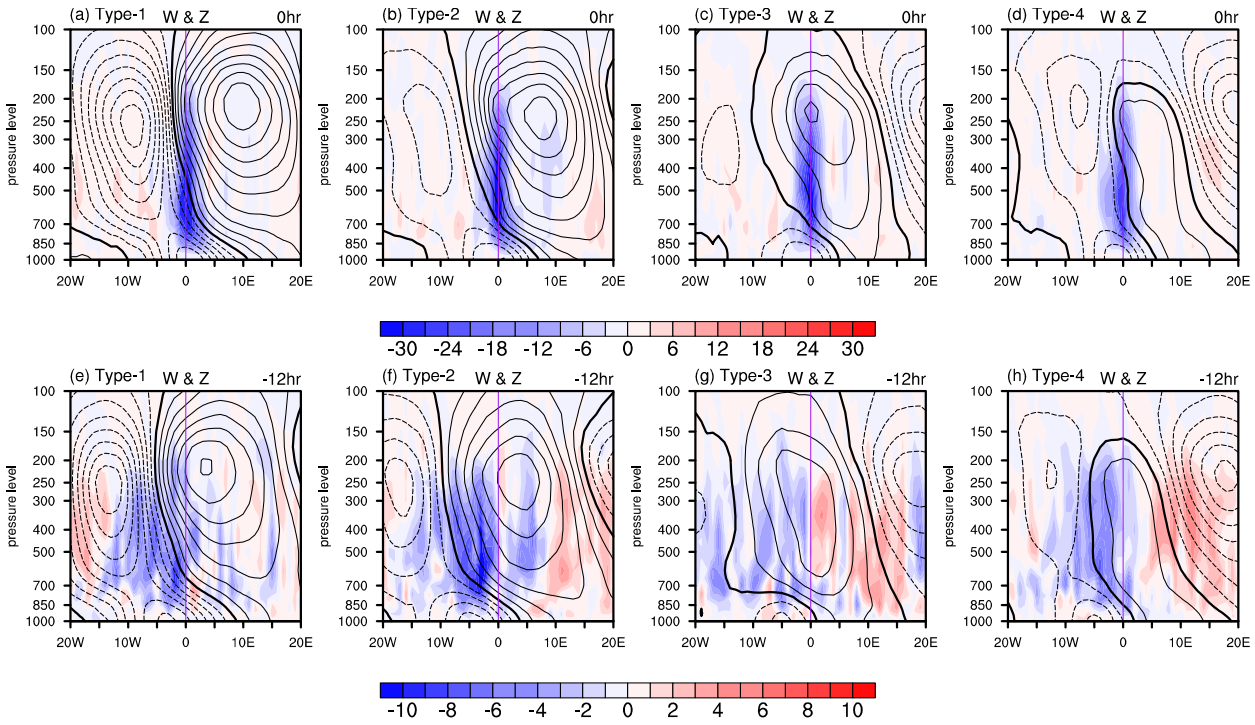


734

735 **Fig. 5** Same as Fig. 4 but for vertical velocity (shading; units: $10^{-2}$ Pa $s^{-1}$) and geopotential height

736 (contour; units: m). The contour interval is 3 m.

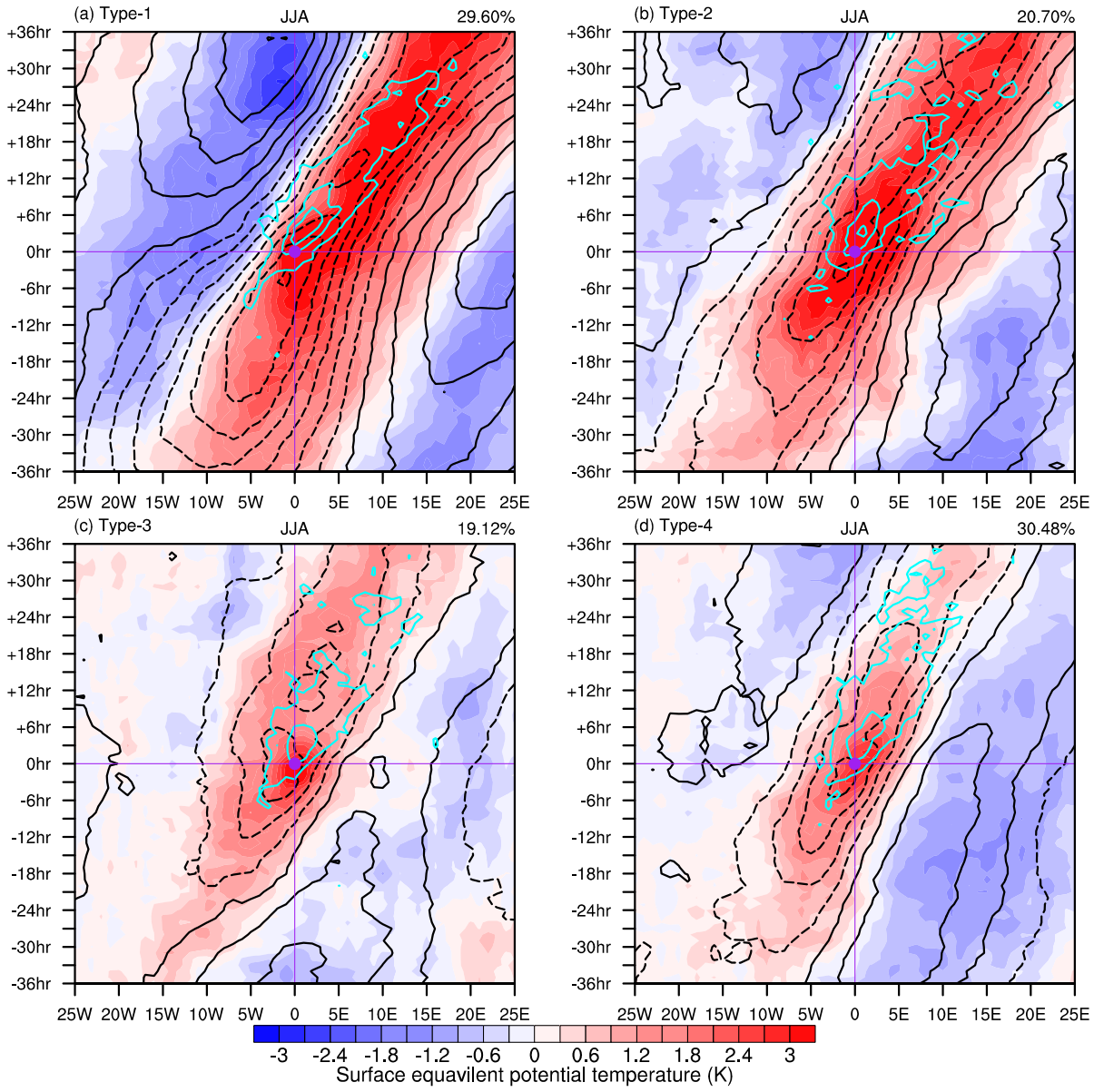


737

738 **Fig. 6** The longitude-time section of convection-centered environments along the latitude of
739 MCSs initiation spanning from the foothill of the Rocky Mountains to the central Great Plains
740 (25°-50°N, 90°-105°W; purple boxes in Fig.1a-d and Fig. 2a-d): surface equivalent potential
741 temperature (shading; units: K), surface pressure (black contour; units: hPa) and precipitation
742 (cyan contour; units: mm day$^{-1}$). The black solid (dashed) lines represent positive (negative)
743 surface pressure, with an interval of 0.3 hPa. The solid cyan lines represent positive precipitation,

744 with an interval of 0.3 mm/day. The purple dot indicates the MCS initiation longitude and
745 moment (0° and 0 hr); E (W) in the x-axis means east (west) of the convection initiation and +
746 (-) in the y-axis means after (before) the convection initiation.

747

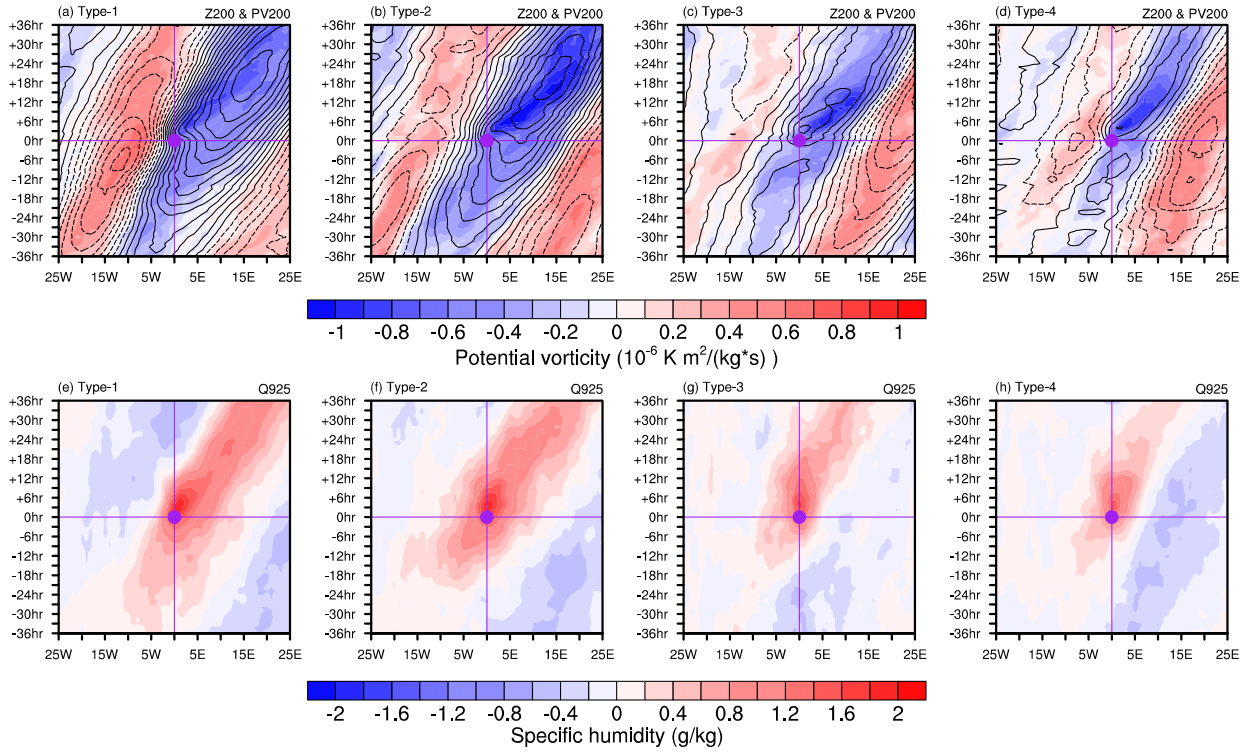


**Fig. 7** The longitude-time section of convection-centered environments along the latitude of MCSs initiation spanning from the foothill of the Rocky Mountains to the central Great Plains (25°-50°N, 90°-105°W; purple boxes in Fig.1a-d and Fig. 2a-d): (a-d) 200 hPa potential vorticity (shading; units: $10^{-6}$ K m$^2$ kg$^{-1}$ s$^{-1}$) and geopotential height (contour: units: m) and (e-h) 925 hPa specific humidity (units: g kg$^{-1}$). In (a-d), the black solid (dashed) lines represent positive (negative) geopotential height, with an interval of 3 m. The purple dot indicates the MCS initiation longitude and moment (0° and 0 hr); E (W) in the x-axis means east (west) of the convection initiation and + (-) in the y-axis means after (before) the convection initiation.

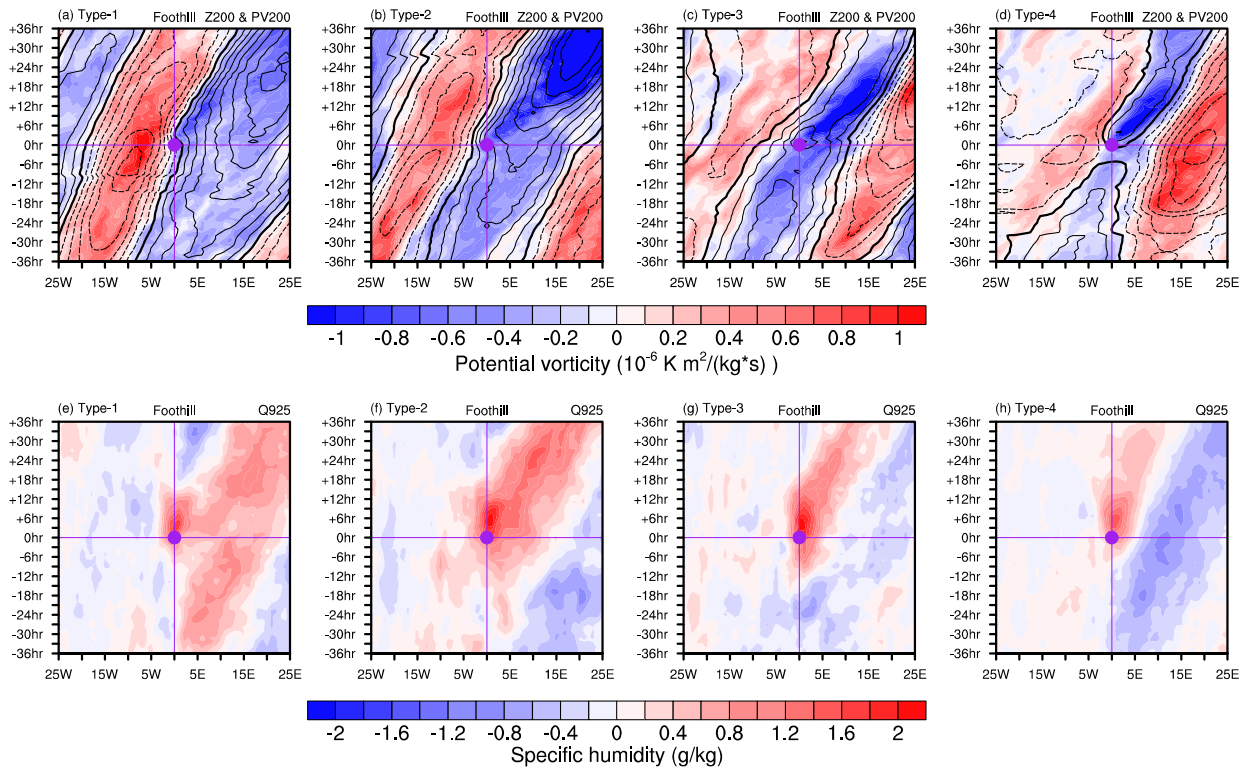


757

758 **Fig. 8** Same as Fig. 7 but for MCSs initiated at the foothill of Rocky Mountain (35°-50°N; 100°-

759 105°W).

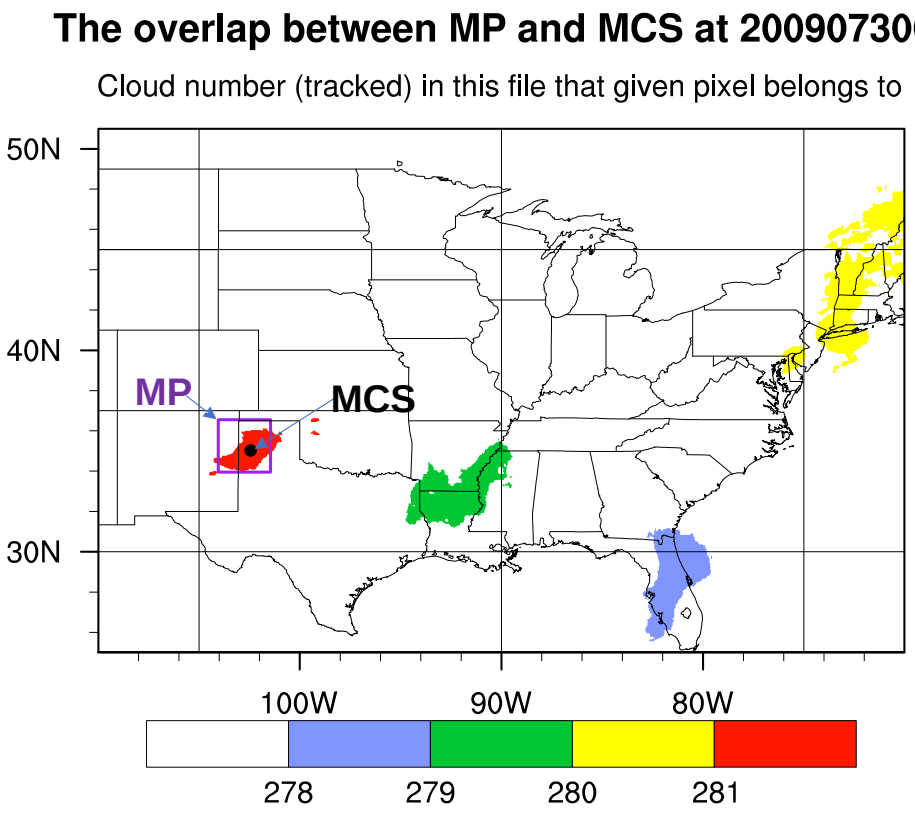


**Fig. 9** Schematic plot of the calculation of overlap between mid-tropospheric perturbation (MP) and MCS based on their respective tracking records. The different colors in this map show the different numbers assigned to each MCS at initiation (shown as cloud numbers). The highest number of 281 is for MCSs initiated at the presented time (2009-07-30-Z01). At the moment of MCS initiation, we search the MP tracking record for a spatial overlap between the new MCS and an active MP (the MP should be initiated before this moment). The spatial extent of each MP is represented by the blue square based on the center coordinate and areal coverage (in terms of the number of the ERA5 grid points) provided by the MP tracking algorithm (circular shape is also tested and gives the same results). As the MP has a threshold and the grid points with lower values are not labeled as MP, the MP area coverage is doubled (we also tested even larger area, but the results are unchanged) to consider the potential impacts of these lower values on the MCS initiation.

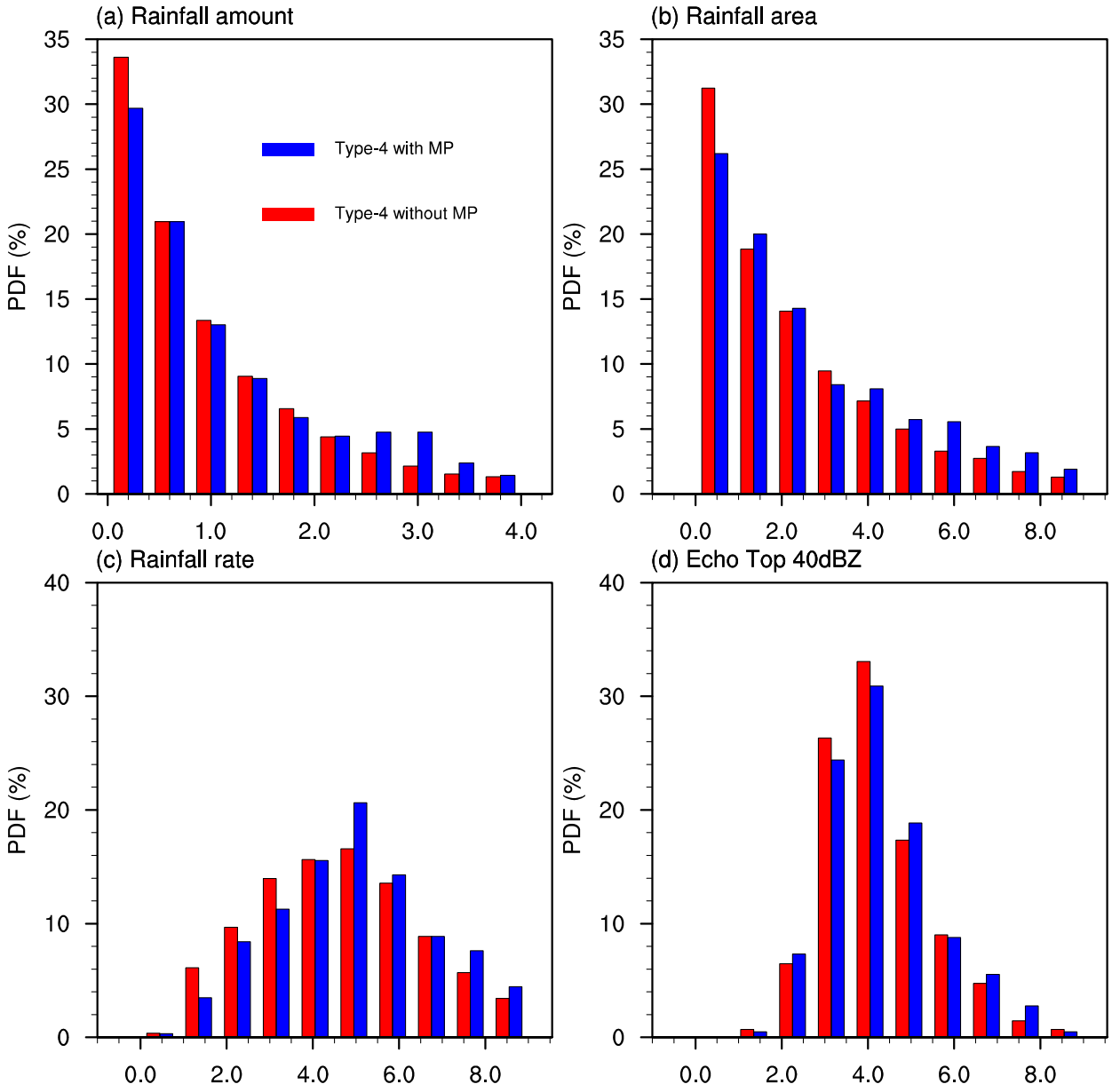


773

774 **Fig. 10** Probability distribution function (PDF) of (a) MCSs rainfall amount (units: $10^4$ mm $hr^{-1}$),

775 (b) MCSs rainfall area (units: $10^4$ $km^2$), (c) MCSs rainfall rate (units: mm $hr^{-1}$) and (d) echo top

776 40 dBZ (units: km) in Type-4 with MP (blue bar) and Type-4 without MP (red bar).